RESEARCH

Digital holographic study of corona wind-assisted evaporation of hydrocarbon from a microliter well

**Digvijay Shukla[1] · Bal Krishan Mishra[1] · Pradipta Kumar Panigrahi[1]**

Abstract

The present study aims to understand the evaporation dynamics of heavy hydrocarbon liquid (cyclohexane) from a circular well cavity under the influence of corona wind. The study explores the effect of corona wind on the modification of vapor phase transport and the evaporation rate from the circular well. Particle image velocimetry is used to characterize the velocity field of the corona wind generated by a needle and plate configuration. Digital holography interferometry is used to decipher the mole fraction distribution of the vapor cloud. Circular well cavities of radius 2.0, 2.5, and 4 mm are studied. The effect of corona wind on the evaporation of different sized well cavities increases with an increase in actuation voltage. The side wall of the cavities influences the distribution of the vapor cloud due to the interaction with the incoming corona wind. More than ten times enhancement of evaporation is observed at 10 kV excitation voltage setting of the corona wind generator. The corona jet-assisted evaporation can be very useful in thin-film evaporative cooling due to its simplicity in design and superior performance.

Graphical abstract
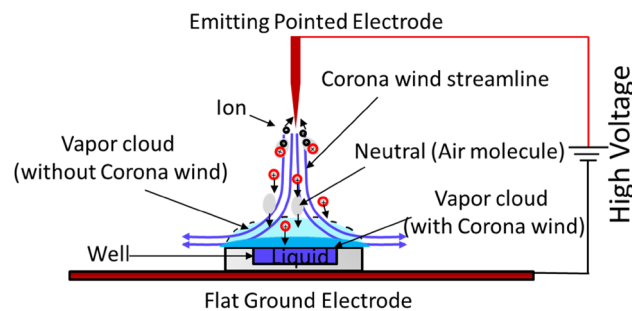
1 Introduction

Heat generation from the electronic components is increasing continuously with increase in number of junctions. Conventional method of heat management such as forced air cooling, heat pipes, etc. is not capable of removing high heat flux from the next-generation electronic devices. Therefore, development of heat transfer enhancement techniques is essential to alleviate the problem due to ever-increasing heat generation in electronic components. Liquid-based thin-film evaporative cooling systems can be a suitable candidate to tackle such high heat flux systems [1, 2]. Thin-film evaporative cooling has an advantage over the two-phase boiling heat transfer systems as latent heat of vaporization can be utilized below the normal boiling point. This can avoid the difficulties associated with large pressure drop and flow instabilities. No significant temperature change is observed in liquid vapor mixture during phase change process leading to small temperature difference. The coolant requirement is also low in an evaporation-based cooling system due to utilization of latent heat of vaporization resulting in lower

✉ Pradipta Kumar Panigrahi
    panig@iitk.ac.in

    Digvijay Shukla
    dvijay@iitk.ac.in

[1] Department of Mechanical Engineering, Indian Institute of Technology Kanpur, Kanpur 208016, India

overall coolant mass requirement of the system. Hence, thin-film-based evaporation cooling systems are ideal for aerospace and space applications.

Evaporation of liquid has potential applications in several fields such as electronic cooling, biological lab on chip applications, thin-film evaporative cooling, drying, painting, etc. This phenomenon has been studied extensively for almost half a decade. Narayan et al. [1] studied gas-assisted thin-film evaporation from confined spaces for the thermal management of hot spots with local heat flux exceeding 600 W/cm^2. Eloyan and Zaitsev [2] studied the evaporating thin layer of liquid film, moving under the action of the gas flow in a flat channel. This system was able to remove heat flux of the order of 1 kw/cm^2. Several aspects of the evaporation process such as substrate properties, liquid properties (single, binary, or nanofluid), heated/non-heated surface, and effect of ambient conditions such as relative humidity have been studied [3]. Vapor phase transport in the gas phase was studied to explore the vapor concentration driven evaporation phenomenon [4–9]. Further research is required to understand the gas-phase transport physics for exploring the possibility of minimizing mass transfer resistance for enhancing the potential of thin-film evaporation-based cooling system.

Application of electrohydrodynamic (EHD) is one of the approaches to enhance thin-film evaporation process. Electrohydrodynamics has shown great success in the applications of fluid flow, convection, boiling, and condensation heat transfer with the advantages in cost saving and environmental friendliness [10, 11]. Vancauwenberghe et al. [12] reviewed the existing literature on the influence of electric field on contact angle, shape, and enhancement of evaporation rate of sessile drops. Takano et al. [13–16] investigated the evaporation of sessile droplet above the Leidenfrost point under the applied voltage varying from 0 to 2000 V, where the droplet is in contact with the electrode and substrate is non-conducting. The applied voltage was set at 300 V, and the substrate temperature was set at 300 °C for ethanol and cyclohexane and 400 °C for water. Maximum enhancement rates (which is defined as the ratio of evaporation time with electric field to the evaporation time without electric field) for ethanol, cyclohexane, and water were equal to 20, 1.3, and 3, respectively [16]. In subsequent study, ethanol and R113 were studied with maximum applied potential equal to 200 V and 2000 V, respectively. The maximum enhancement rates achieved were 7.6 and 2.8 for ethanol and R113, respectively [13]. Authors qualitatively observed that the effect of electric field on non-polar liquids is lower compared to that of polar liquids. This may be attributed to the larger charge relaxation time for former. To further investigate the matter, author studied the critical voltage and response time necessary to render the surface instability of horizontal free surface of non-polar liquid with long relaxation time. They

concluded that response time for the surface instability at some critical voltage is shorter than the charge relaxation time [14, 15]. Bateni et al. [17] studied the effect of electric field on contact angle and surface tension of the sessile droplets. Droplet is placed within the parallel plate capacitor arrangement and electric field is applied between electrodes. They observed increase in the contact angle of polar liquids such as alcohols. However, no significant change is observed in the non-polar liquids such as alkanes with increase in the electric field. Stronger change in contact angle is observed for liquids with long molecules. Polarity of the electric field is not found to be an underlying factor.

Deng et al. [18] studied the charged droplet impact and evaporation on a conducting substrate produced by electrospraying of ethanol. They concluded that image force experienced by the droplet plays significant role on the post-impact history if sufficient residual charge is available in the droplet after impact. If substrate temperature remains at or above boiling point, then this image force prevents the rebound and leads to the flattened sessile droplet which increases the evaporation rate. When substrate temperature reaches above the Leidenfrost point, image force prevents the bouncing of the droplet from the surface. Scaling analysis revealed that the advantage of image force in case of charge droplet does not always help in preventing the rebound. It is only useful for smaller size picoliter droplets not for larger, nanoliter droplets.

Gibbons et al. [19] studied the local heat transfer effect of a sessile droplet placed on a heated substrate under a static electric field. The electric field strength is varied as 0, 5, 10, and 11 kV/cm. With increase in the electric field, decrease in the contact angle is observed, while cooling profile, peak convective heat flux, and the radial location of this peak are independent of the applied electric field. Fan et al. [20] studied the evaporation of charged droplets with different electrical conductivity on the hydrophobic substrate. Droplet is placed between two parallel plate electrodes where lower electrode is hydrophobic, and voltage is applied at lower electrode and upper electrode is grounded. They observed increase in evaporation rate with increase in applied electric field and evaporation of charged droplet can be divided into two stages: the stationary and accelerated stage. At the same applied voltage, evaporation time of water droplet is almost double compared to the hydrochloric acid (HCl) droplet.

Xu et al. [21] studied the water droplet evaporation on heated Teflon-coated copper surface in the presence of non-uniform electric field generated by needle and plate configuration. They observed that both increase in external electric field strength and surface temperature enhance droplet evaporation with a maximum enhancement ratio of 6.8. Enhancement in evaporation is attributed to the mechanism of non-uniform electric field due to corona wind blowing, surface tension weakening, and molecular orientational alignment.

External convection produced by the corona wind is a promising enhancement method in drying applications due to its lower energy consumption [22–24]. The mechanism of this enhancement is attributed to a secondary flow induced by the electric body force. When a high electric field is maintained between two electrodes with dissimilar curvature (i.e., one is sharp and the other is blunt), air molecules near the sharp electrode become ionized. The ions are accelerated under the intense electric field and move towards the collecting blunt electrode. This migration leads to further collision between ions and neutral air molecules, transferring momentum from ions to neutral air molecules. A bulk of air flow is thus created, which is customarily called ionic wind or corona wind [25]. Bin et al. [26] studied the effect of external horizontal air flow on the evaporation of methanol droplets of different radius placed on the Teflon surface. The evaporation rate increases with increase in air velocity.

The above literature review shows that most of the studies performed till date on the effect of electric field on droplets are mainly focused on electrowetting phenomenon where droplet is placed on a non-conducting substrate. Two configurations are primarily used. In one configuration, a needle electrode is in contact with the droplet placed on a non-conducting substrate. In the other configuration, droplet is placed between two parallel plates of a capacitor and the plate on which droplet is placed is kept insulated. It is observed that presence of electric field increases the wettability and anchors the shape of a droplet. Lower contact angle leads to higher evaporation rate.

From the above literature review, it can be concluded that effect of non-uniform electric field-induced corona wind on the evaporation of a volatile and non-polar hydrocarbon of microliter volume cavities is not available in the literature. The understanding of thin-film evaporation phenomenon and vapor phase transport under the effect of external flow is also not well understood. Therefore, the present study investigates the effect of corona wind induced external convection on the evaporation and vapor phase transport of heavy hydrocarbon (cyclohexane) from a microliter circular well cavity. Digital holographic interferometry and particle image velocimetry have been used for characterization of concentration and velocity field, respectively. Vapor cloud of liquid evaporating from the well cavity under the influence of corona jet is compared to the natural evaporation case to understand the physics of mass transfer in the presence of external convection.

2 Experimental details

The experimental details for the present study are presented below in the following sequence: (a) corona wind and micro-well arrangement, (b) digital holography setup, (c) particle image velocimetry setup, (d) data analysis, and (e) uncertainty analysis.

2.1 Corona wind and micro-well arrangement

The micro-well arrangement with corona wind generator setup is shown in Fig. 1. Corona wind is generated using a pin-plate geometry, where potential difference is applied between the pin and the plate. The distance between the ground plate and the needle tip is equal to 25 mm. Diameter of the steel needle is 0.7 mm with the tip radius of 0.1 mm. A square copper plate of 3 mm thickness and 75 mm width is used as a ground plate. High-voltage power supply (GBS electronics Germany) is used to supply positive high voltage at the needle tip. Voltage can be varied from 0 to 30 kV. Circular wells are fabricated at the centre of the plexiglass piece ($20 \times 20 \times 10$ mm^3 size). The radius of circular wells is varied as 2, 2.5, and 4 mm having depth of 2 mm. Cyclohexane is used as working fluid. The high viscosity (1 cP) of cyclohexane prevents splashing of the liquid from the well cavity by the striking corona wind. All experiments are conducted at the ambient temperature of 25.5 ± 0.5 °C with relative humidity between 70 and 80%. Liquid is filled inside
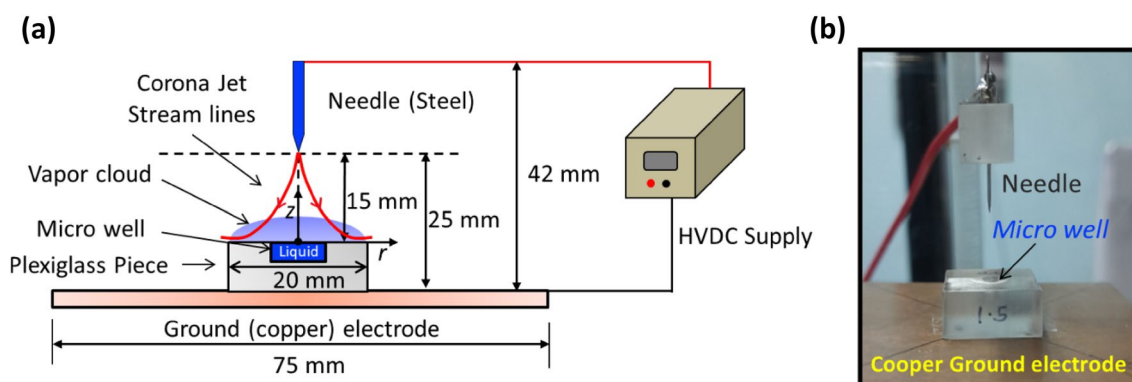

Fig. 1 **a** Schematic of the experimental arrangement for corona wind-assisted micro-well evaporation and **b** snapshot of the arrangement

the cavity and positive DC potential is applied between the needle and the plate for initiating the corona wind-assisted evaporation.

2.2 Digital holography setup

Figure 2a shows the experimental arrangement for holographic measurement of vapor cloud behaviour. Digital holographic interferometry is used to measure the vapor mole fraction above the evaporating well cavities. The total time of evaporation from the cavity is determined using the on-axis digital holography. The liquid is filled inside the cavity through a micropipette. Interferograms are recorded at the time interval of 100 ms until liquid is completely evaporated, which is determined based on transient behaviour of interferogram. Off-axis digital holographic interferometry is used to measure the phase shift produced due to the presence of vapor cloud above the cavity. This information is analysed for understanding the vapor phase transport and its modification due to the presence of corona wind.

The holographic interferometry setup consists of a He–Ne laser of wavelength, 632.5 nm with a beam diameter of 0.98 mm. This beam passes through the spatial filter and subsequently gets collimated by a Plano convex lens. The incident beam is subsequently divided into two separate beams with the help of a beam splitter and recombined at second beam splitter. The intensity pattern from the second beam splitter is recorded by the CCD camera (BASLER A317 782×582 pixels) through a zoom lens (Micro NIK-KOR). The beam which passes above the evaporating well is called object beam and the other part is called as reference beam. The refractive index variation produced due to the difference in refractive index of the vapor cloud in the object beam and reference beam is recorded in the form intensity pattern which is called as digital hologram and recorded by the camera. Further data processing is carried out to obtain the phase shift information which represents the vapor cloud concentration.

2.3 Particle image velocimetry setup

The flow field generated due to corona wind can be characterized using the particle image velocimetry (PIV) technique. The PIV technique has been extensively used to study the flow generated by the electrohydrodynamic-based flow control actuators [27]. In the present investigation, we have used a custom time-resolved PIV (TR-PIV) system to measure the flow field generated by the needle and plate configuration under the action of high voltage. Figure 2c shows the experimental arrangement used for the PIV measurement. It comprises of a
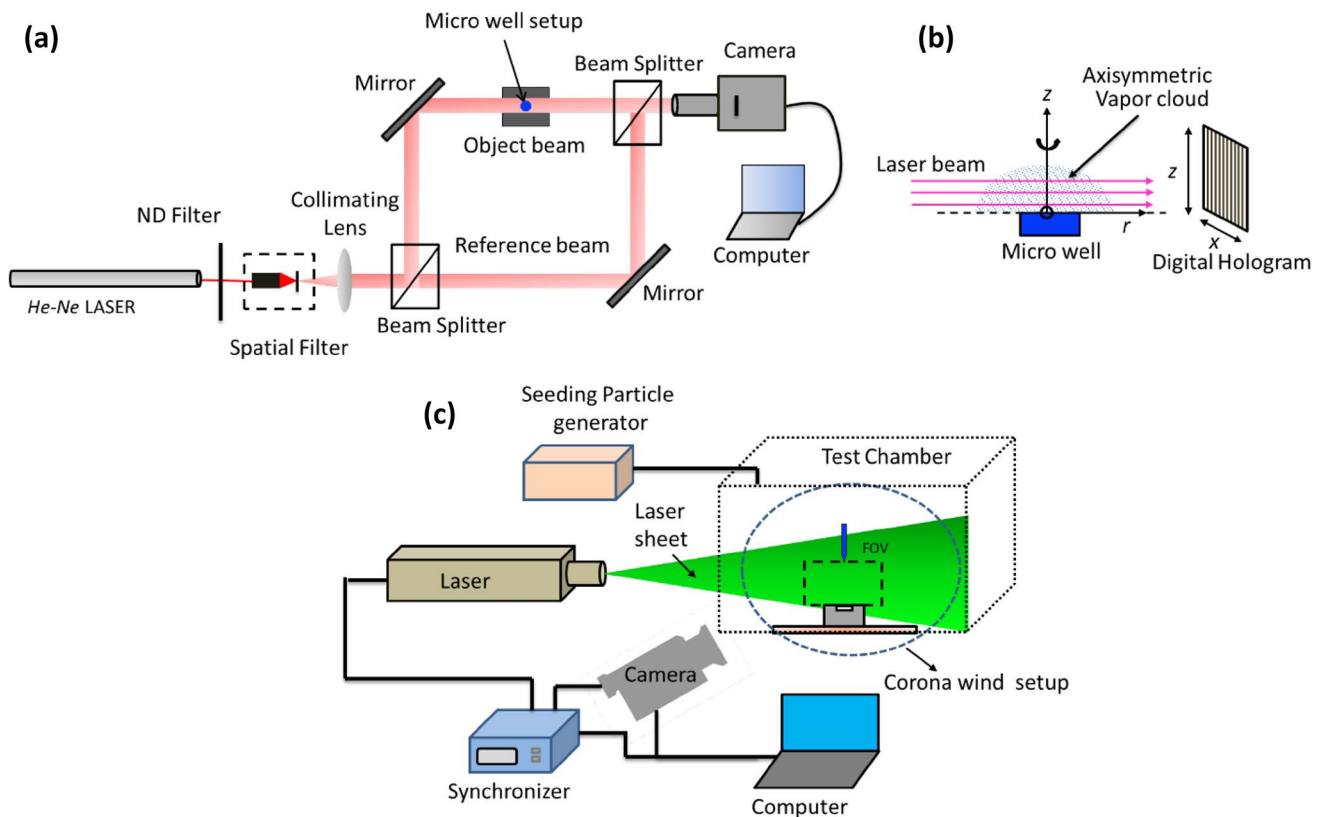

Fig. 2 Schematic of **a** digital holographic interferometry setup, **b** the co-ordinate system, and **c** particle image velocimetry setup

high-speed laser, synchronizer, high-speed camera, and atomizing seeding generator. The corona wind generator is placed inside a closed chamber, and the entire chamber is seeded with smoke particles. More details about the TR-PIV system and experimental procedure can be found in our previous work [28]. The PIV images were recorded with a resolution of 800×600 pixels equal to 27.6×20.7 mm^2 in physical units. The sampling rate of 3200 frames per second (fps) was used for 6 and 8 kV actuation and 4000 fps was used for 10 kV actuation. The image pairs are downsampled by a factor of 28, i.e., it becomes 114.3 fps for 6 and 8 kV actuation and 142.9 fps for 10 kV actuation. The PIV images were processed in commercial software (VidPIV 4.6 supplied by Oxford Lasers). A cross-correlation algorithm is applied on a window size of 64×64 pixels^2, and then, an adaptive cross-correlation scheme is applied on a reduced window size of 32×32 pixels^2. The cross-correlation and adaptive cross-correlation schemes were implemented with an overlap of 50%. The final vector field is obtained using the local velocity filter followed by the interpolation of outliers. The flow field obtained from PIV has an effective resolution of 0.552 mm.

2.4 Holographic data analysis

Fourier transform profilometry algorithm is used to extract the phase shift due to the vapor cloud above the evaporating well [29]. A reference hologram was recorded before filling the liquid inside the cavity to overcome any aberrations produced by the optical setup. The phase field obtained from the object hologram is subtracted by the phase field obtained from the reference hologram. The resulting phase filed is called wrapped phase map due to the vapor cloud. Because the obtained phase shift map is wrapped between 0 and 2π due to the use of arctan function in the algorithm processed in MATLAB platform. Therefore, Goldstein algorithm is used for phase unwrapping [30]. A continuous distribution of the phase shift ($\Delta\phi$) is obtained, which describes the nature of vapor cloud and vapor transport from the cavity. The measured phase shift is a projection of the total phase shift along the path length, as shown in Fig. 2b. Therefore, an inverse Abel inversion is carried out for tomographic reconstruction, which gives the axisymmetric refractive index filed ($\Delta\eta$). Fourier–Hankel algorithm is used for tomographic reconstruction [31]. Detailed procedure of data reconstruction process has been explained in our previous study [8]. The refractive index field can be converted into the respective vapor mole fraction (χ) using the following equation [7]:

$$\chi = \frac{1}{\eta_v - \eta_a} \Delta\eta. \tag{1}$$

Here, η_v and η_a are the refractive index of pure vapor and air, respectively. The refractive index of pure vapor of cyclohexane (η_v) is 1.001688 and air is 1.000268 at 25 °C for the wavelength of 632.8 nm [32, 33].

2.5 Uncertainty analysis

Bias error sources such as electronic noise and other environmental effects during holographic data inversion are eliminated by subtraction of object field image from the reference intensity image. The other sources of error are the error in setting the initial volume of liquid inside the cavity, convection inside the room, fluctuation of the incident light, and image acquisition error. We have carried out repeated experiments to minimize any random error due to instrumentation noise and environmental conditions. Error in the measurement of average evaporation rate can be attributed to the initial volume setting of the micropipette and the calculation of the total time of evaporation from interferogram visualization and variation in the ambient conditions. Three sets of experiments are conducted for each case and average of the total evaporation time is reported along with the standard deviation. Good match between two sets of PIV measurements and averaging of 200 number of piv images is carried out to obtain the average velocity field information. The maximum error in velocity measurements based on repeatability study is equal to 5%.

3 Results and discussion

Understanding the modification of vapor cloud and vapor phase transport due to action of ionic wind is the main focus of this paper. Effect of ionic wind induced external convection on the microliter well cavities of different radius has been investigated at various applied potentials. The results are discussed in the following sequence: (a) evaporation rate, (b) velocity field, and (c) vapor cloud characteristics.

3.1 Evaporation rate

Figure 3 shows the total evaporation time of liquid evaporating from the microliter volume circular well cavities of different radius with respect to applied voltage between the needle and ground electrode. The total evaporation time increases with increase in radius of the cavity. There is a sharp drop in evaporation time at an actuation voltage of about 4 kV. Subsequently, the evaporation time shows a slow decrease with respect to increase in actuation voltage.

The value of the electric field required to ionize the gas near the tip of the needle can be obtained from the Peek's formula for pin and plate setup [34, 35] as
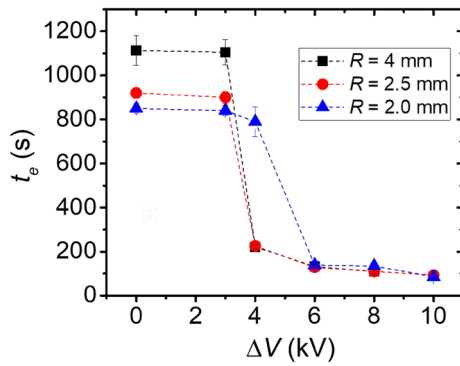
Fig. 3 Variation of total evaporation time (t_e) with respect to applied potential (ΔV) across electrodes as a function of microliter well cavities radius (R)

$$E_w = 3.23 \times 10^6 \left(1 + \frac{2.62 \times 10^{-2}}{\sqrt{r}} \right). \tag{2}$$

Here, r is the needle tip radius in (m) and E_w is in (V/m). The voltage required for the initiation of corona discharge (V_w) can be calculated using the following expression [36], where L is the distance between the needle tip and the ground electrode in (m) and V_w is in (V):

$$V_w = \frac{E_w r \ln\left(4L/r \right)}{2}. \tag{3}$$

The initiation voltage for generation of corona wind in pin-plate configuration is calculated as 4.038 kV. It can be observed from Fig. 3 that before the inception of ionic wind (below 4 kV), no significant change is observed in the total time of evaporation (t_e) due to the application of electric field for all cavities. This demonstrates that electrical body force has negligible effect on the evaporation rate enhancement. When actuation voltage is higher than the onset voltage of corona wind, significant reduction in the total evaporation time is observed.

Figure 4a presents the variation of average evaporation rate per unit surface area with respect to applied potential for the microliter cavity of different radius. Average evaporation rate before the initiation of corona wind, i.e., at actuation voltage less than 4 kV is almost similar for all cavity size cases. At higher actuation voltage, the average evaporation rate of 2 mm size cavity is slightly lower till 8 kV actuation. At highest actuation voltage of 10 kV, the average evaporation rate reduces with increase in cavity radius. Lower average evaporation rate for smaller size cavity below 8 kV actuation can be attributed to the greater obstruction effect by the edge of the well to the corona wind flow.

Enhancement in the average evaporation rate, E^*, is defined as a ratio of average evaporation rate from the cavity with actuation to that without actuation. Variation of E^* with respect to the applied voltage for the microliter cavities of different radius is shown in Fig. 4b. No enhancement in the evaporation rate is observed before initiation of corona wind which indicates that the non-uniform electric field does not affect the evaporation rate for non-polar liquids [17]. Once corona jet is generated, external convection induced in the gas phase sweeps the vapor from the gas domain which significantly increases the evaporation rate. Almost ten times increase in evaporation rate is observed at the applied potential of 10 kV for all the cavities. This demonstrates the effectiveness of corona wind on thin-film evaporation-based cooling systems. Higher values of E^* are observed for the larger radius well cavity ($R = 4.0$ mm) compared to smaller radius cavities. This effect is more significant at lower applied voltages. This can be attributed to the greater size of the corona jet which cannot be completely utilized by the smaller radius cavity. Some portion of the corona jet falls outside the well cavity and does not contribute to forced convection mass transfer. It may be noted that Xu et al. [21] observed maximum enhancement ratio of 6.8 for

Fig. 4 **a** Variation of average evaporation rate per unit area (E_{avg}) and **b** evaporation rate enhancement ratio (E^*) with respect to the applied potential (ΔV) between needle and ground electrode as a function of circular well cavities radius (R)
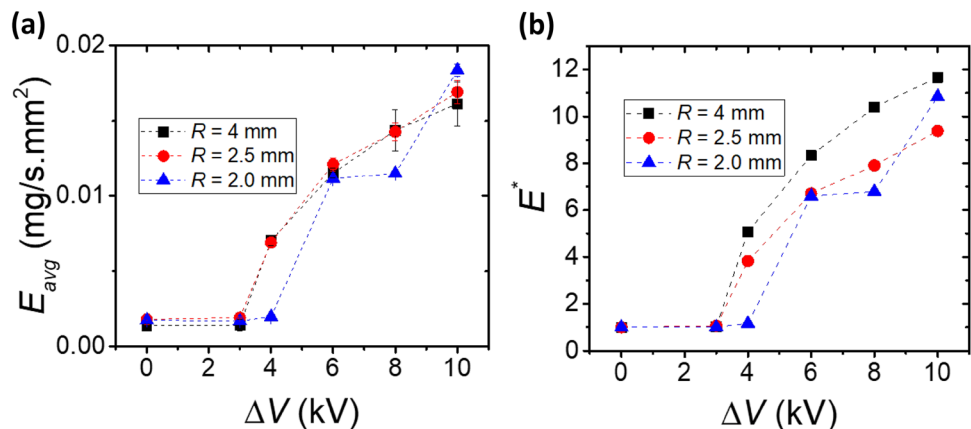
sessile water droplet evaporating from a heated substrate under the presence of non-uniform electric field.

3.2 Velocity field

Figure 5 shows the time-averaged flow field generated by the needle and plate configuration due to the corona wind as a function of actuation voltage (6 kV, 8 kV, and 10 kV). The velocity vectors are superimposed on the iso-contours of radial (u_r) velocity field. The flow is initiated from the electrode tip, which acts like a point source. This is evident from the axial velocity distribution, which is aligned with the axis of the needle. The initiation of axial velocity at the tip of the electrode tip is accompanied with

Fig. 5 Time-averaged radial (u_r) velocity (left column) and axial velocity (u_z) (right column) contour superimposed on velocity vector field and velocity profile at selected normal locations ($z = 3$ mm and 12 mm) as a function of actuation voltages
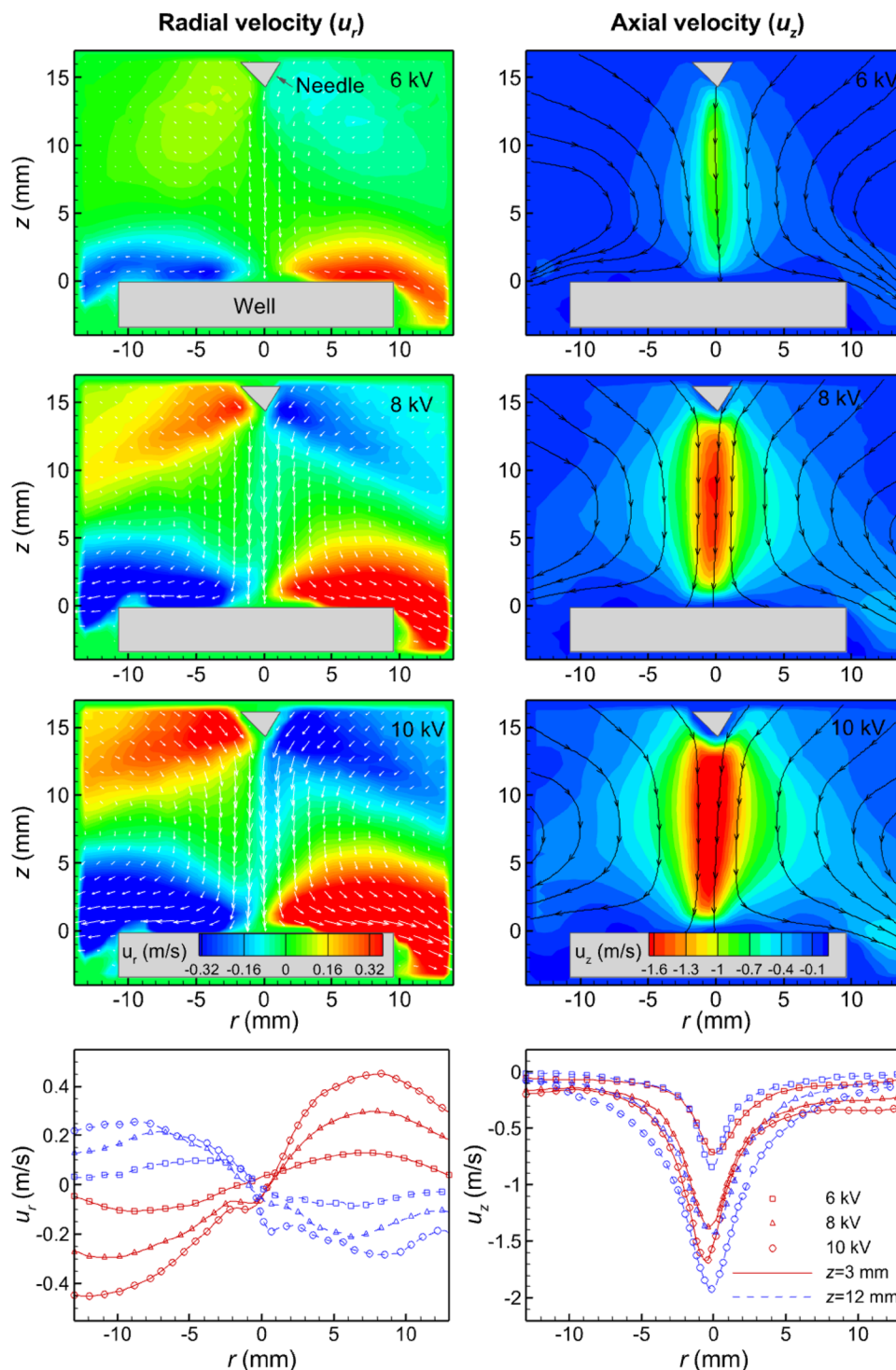
higher radial velocity around the electrode tip region. The absolute maximum of axial velocity magnitude is equal to 0.95 m/s, 1.64 m/s, and 2.01 m/s for 6 kV, 8 kV, and 10 kV actuation, respectively. The flow from the surrounding medium towards the electrode takes place to satisfy mass continuity. The magnitude of both axial and radial velocity increases with increase in actuation voltage. The width of corona wind jet increases in the axial (z) direction. This may be attributed to the entrainment of fluid from the ambient as the corona wind jet travels towards the well region.

The corona wind jet impinges on the substrate surface and the circular well. The impingement process is accompanied with higher radial velocity in the near wall region of the substrate. The direction of radial velocity in the substrate region is opposite to that in the tip region of the electrode due to difference in nature of the process. The magnitude of radial velocity in the impingement region also increases with increase in actuation voltage. The average magnitude of radial velocity in the impingement region is higher than that near the electrode tip region. This may be attributed to the entrainment of ambient fluid from the ambient as corona wind traverses from the pointed electrode region. The entrainment effect can also be confirmed from the axial velocity profile at 3 mm and 12 mm shown at the bottom of Fig. 5. The axial and radial velocity profile shown at $z = 3$ mm and 12 mm clearly demonstrates the effect of actuation voltage. The streamline plots are superposed on the axial velocity contour in the right column of Fig. 5. The streamline plot shows the streamline entering perpendicular to the well at the centerline region. The streamlines are aligned parallel to the tip surface in the entrainment region. Similarly, the streamlines are aligned to the substrate in the impingement region.

3.3 Vapor cloud characteristics

Figure 6 presents the snapshots of the interferograms at various non-dimensional time ($t^* = t/t_e$, where t is any time instant and t_e is the total time of evaporation) as a function of applied voltage for the microliter well cavity of radius 4 mm. Flat disk-shaped vapor cloud is observed for the no actuation case (0 kV). The number of fringes reduces with increase in time instant. This may be attributed to the reduction in evaporation rate with time and diffusion of vapor to the ambient. At 4 kV, corona wind is initiated leading to change in shape of the vapor cloud at $t^* = 0$. The downward deflection of the fringe at the centre region of the well may be attributed to the deflection of the liquid interface and vapor cloud by the impinging corona jet. The maximum deflection at the centre region corresponds to the maximum axial velocity at the centre of the corona wind jet, as shown in Fig. 5. The fringe outside the well region can be attributed to the presence of vapor cloud outside the interface due to the downward movement of vapor cloud as the vapor is heavier than the ambient air and the radial displacement of vapor due to radial velocity of corona wind (see Fig. 5). The radial spread of the vapor cloud also increases due to the corona wind compared to the no actuation case. The thickness of the vapor cloud, i.e., fringe location reduces with progress in time. The thickness of the vapor cloud near the centre of the well reduces with increase in actuation voltage due to increase in corona wind velocity. Corona jet strikes liquid–vapor interface from the top and the vapor leaves from the corner of the cavity which can be noticed from the shape of iso-contours. The fringes near the interface disappears with completion of evaporation. The change in the shape of interferogram with time may be attributed to decrease in interface height due to evaporation. The shape of fringes around the edge of the cavity is a function of actuation voltage as the corona wind deflected from the bottom of the well is deflected at different angle depending upon the velocity of corona jet. The

Fig. 6 Time evolution of vapor cloud interferogram as a function of applied voltage for cyclohexane evaporating from the well cavity of 4 mm radius. Field of view is equal to 5.8 mm×17.5 mm
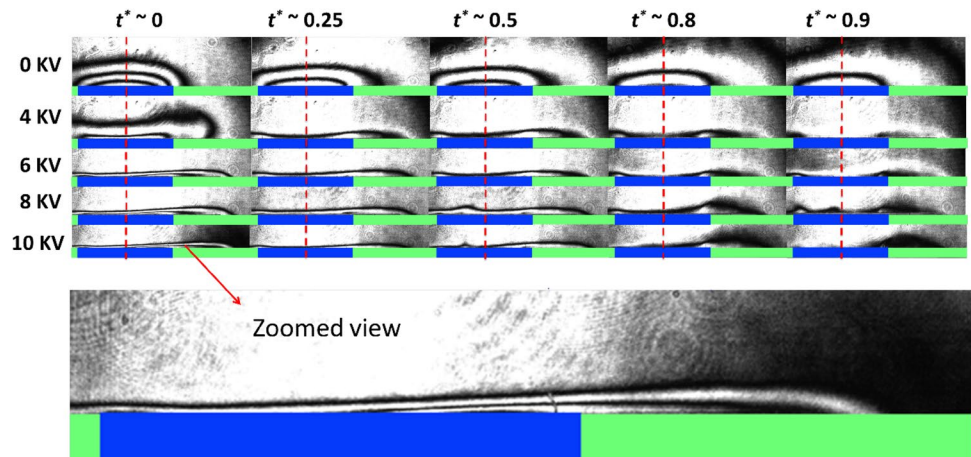
random fluctuations in the fringes are observed, which can be attributed to the fluctuations of the liquid–vapor interface due to the fluctuations of corona wind.

Figure 7 shows the normalized projected phase shift ($\Delta\phi^*$) and corresponding normalized vapor mole fraction maps (χ^*) for cyclohexane evaporating from the microliter well cavities of different sizes at various applied potential for the initial time period ($t \sim 0$ s). Here, normalization is performed with respect to the respective maximum values at the interface ($z = 0$ mm). Vapor cloud shape changes as the corona wind interacts with vapor cloud ($\Delta V \geq 4.0$ kV). Vapor mole fraction reduces at the interface region ($0 \leq r < R$) and vapor escapes from the edge of the cavity ($r \approx R$). As the velocity of corona jet increases at higher actuation voltage,

vapor mole fraction inside the cavity reduces to almost zero at the interface region and vapor only escapes from the edge of the cavity ($r \approx R$). The overall width of the vapor mole fraction contour increases with increase in cavity size. The shape of the vapor cloud above the substrate surface and outside the well region is a function of both well size and actuation voltage. It may be noted that the high radial velocity in the impingement region is a function of the actuation voltage (see Fig. 5). The concentration distribution in Fig. 6 is a combined effect of interaction between incoming corona wind and the vapor cloud escaping from the well interface. The vapor mole fraction distribution outside the edge of the cavity shows two peak regions on the substrate surface at higher actuation voltage (6, 8, and 10 kV). This two-peak

Fig. 7 Normalized phase shift in projected z–x plane and the normalized vapor mole fraction contour in z–r plane of liquid evaporating from wells of different radius ($R = 2.0$, 2.5 and 4 mm) at time $t \sim 0$ s as a function of applied voltage. Field of view is 3.8 mm × 25.4 mm. Normalization is performed with respect to the respective maximum value at the interface for both phase shift and vapor mole fraction
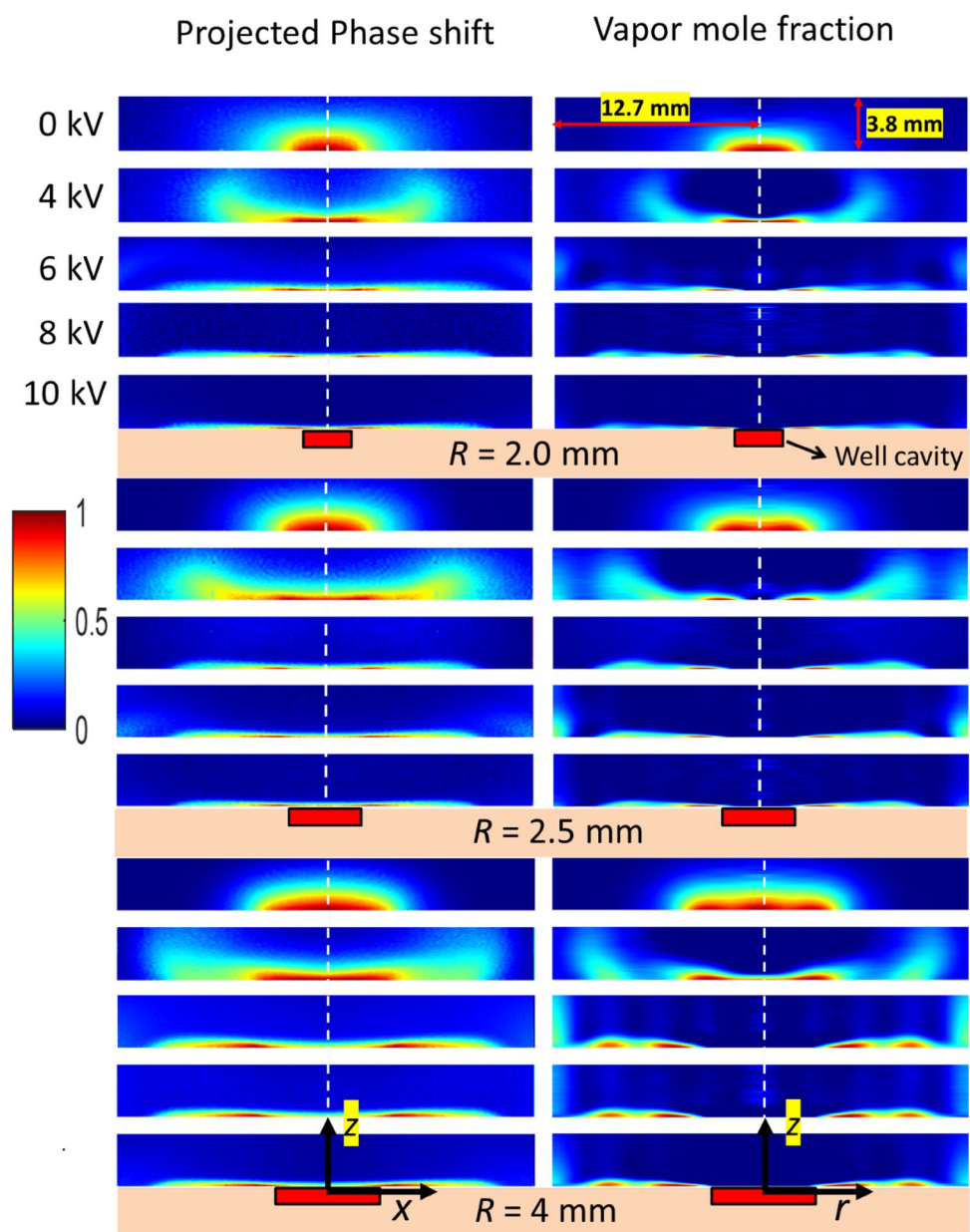
behaviour correlates with the axial velocity contour shape near the substrate region in Fig. 5.

Figure 8 shows the radial vapor mole fraction profile at three different z-locations, i.e., $z = 0$ µm (near liquid–vapor interface), $z = 240$ µm, and $z = 480$ µm above the well surface for initial time period. It can be seen that the values of vapor mole fraction near the liquid vapor interface are close to the saturated value of vapor mole fraction ($\chi = 0.128$) of cyclohexane at 25 °C for the no actuation case. This confirms the capability of holographic interferometry technique to accurately measure the vapor concentration inside the vapor cloud. High vapor mole fraction above the well region due to evaporation of liquid from the well drops in the radial direction for no actuation case. The peak value of the vapor mole fraction is observed at the centre of the well for 2 mm well size case. However, the peak is observed at the off-centre location around the edge of the cavity for 2 mm and 4 mm size cavity case. This may be attributed to negative buoyancy force because of vapor being heavier than air.
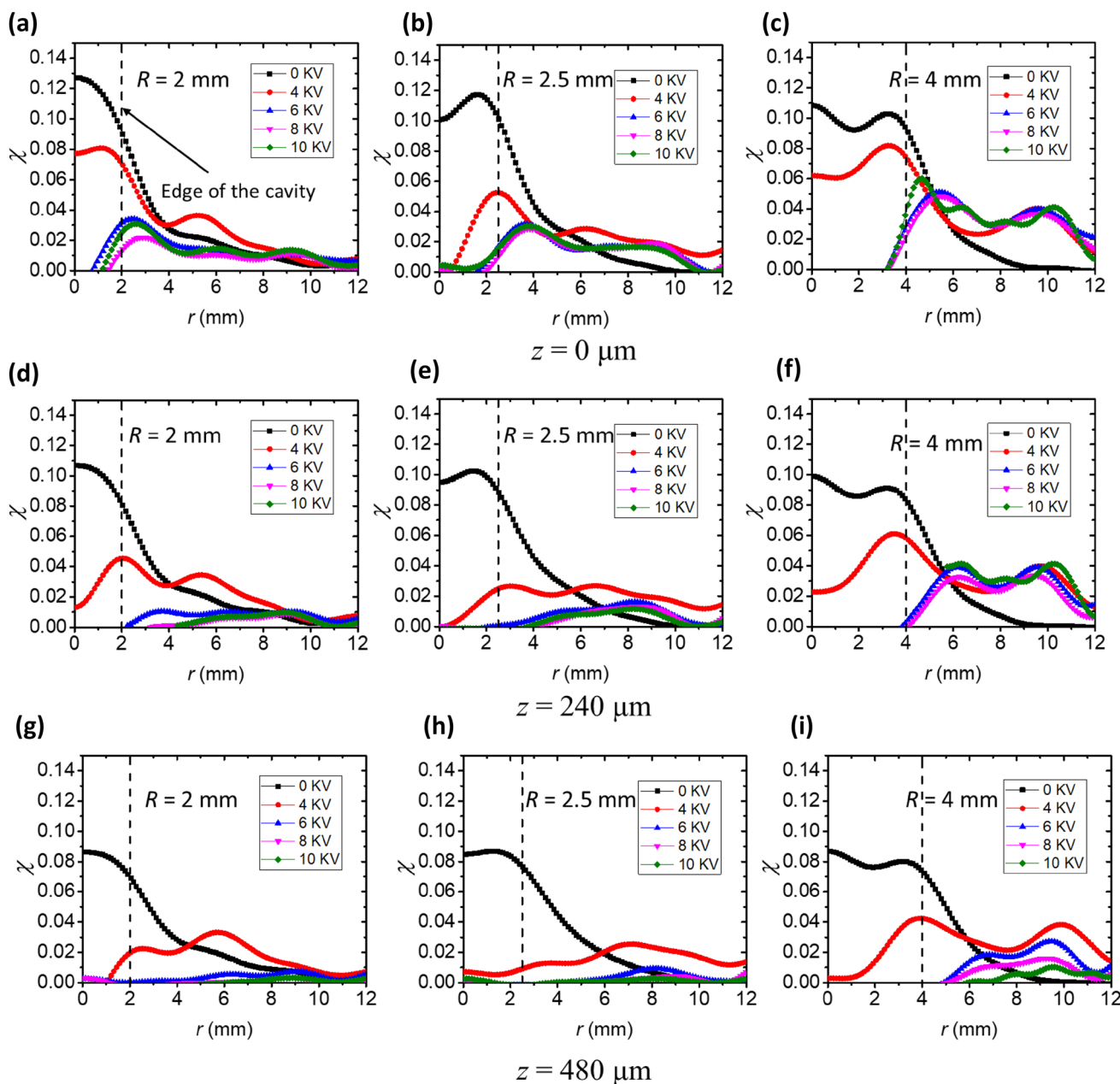

Fig. 8 Vapor mole fraction profile in the radial direction for different well cavity size ($R = 2$, 2.5 and 4 mm) as a function of actuation voltage during the initial time period ($t \sim 0$ s) at various normal distance from the liquid–vapor interface: $z = 0$ µm (**a**, **b** and **c**), $z = 240$ µm (**d**, **e** and **f**), and $z = 480$ µm (**g**, **h** and **i**)

Vapor mole fraction values are lower in the centre of the well region for corona wind case compared to no actuation case as the corona wind displaces the vapor cloud in radial direction. The vapor mole fraction reduces at the centre and increases towards the edge of the well for the actuation case. This is attributed to the effect of corona jet impinging on liquid–vapor interface, which displaces the vapor cloud in the outward direction, i.e., towards the edge region of the cavity. The spread of the dual peak increases with increase in the well cavity size due to higher distance of the edge from the centre of the well. The spread of the vapor cloud in radial direction also increases with increase in actuation voltage due to greater momentum of the corona wind. The dual peak in the mole fraction distribution at higher actuation voltage is attributed to the competition between upward motion of the vapor plume and the downward motion of the heavier than air vapor.

4 Conclusions

The present study investigates the evaporation and vapor phase transport from microliter well cavities of different sizes under the influence of ionic wind jet. The ionic wind jet is generated when high voltages are applied between the needle and plate electrodes. Particle image velocimetry is used for the characterization of the corona wind. Digital holographic interferometry is used for characterizing the vapor concentration distribution of the vapor cloud. Goldstein algorithm is used for phase unwrapping and Fourier Hankel algorithm is used for tomographic reconstruction of mole fraction distribution. The cavity sizes are varied as 2, 2.5, and 4 mm. The actuation voltage is varied between 2 and 10 kV. Some of the important observations from the present study can be summarized as follows:

1) Corona wind is an effective methodology for thin-film evaporative cooling. More than ten times enhancement of evaporation rate has been demonstrated.
2) Ionic wind modifies the vapor cloud distribution above the circular well cavity leading to vapor cloud thinning and deflection of the vapor cloud in the radial direction.
3) Magnitude of the corona wind increases with increases in actuation voltage. It produces a wall jet like flow; part of which impinges on the liquid interface and part of which travel in the radial outward direction transporting the vapor.
4) The actuation voltage of the corona jet generator for a given well cavity size needs to be optimized for maximizing the performance of the evaporative cooling system.

Declarations

Conflict of interest The authors declare no conflict of interest.

References

1. S. Narayanan, A.G. Fedorov, Y.K. Joshi, Nanoscale Microscale Thermophys. Eng. **13**, 30–53 (2009)
2. K.S. Eloyan, D.V. Zaitsev, J. Phys. Conf. Ser. **1105**, 012084 (2018)
3. D. Brutin, V. Starov, Chem. Soc. Rev. **47**, 558–585 (2018)
4. P. Kelly-Zion, C. Pursell, S. Vaidya, J. Batra, Colloids Surf. A Physicochem. Eng. Asp. **381**, 31–36 (2011)
5. P. Kelly-Zion, C.J. Pursell, N. Hasbamrer, B. Cardozo, K. Gaughan, K. Nickels, Int. J. Heat Mass Transf. **65**, 165–172 (2013)
6. P.L. Kelly-Zion, C.J. Pursell, R.S. Booth, A.N. VanTilburg, Int. J. Heat Mass Transf. **52**, 3305–3313 (2009)
7. S. Dehaeck, A. Rednikov, P. Colinet, Langmuir **30**, 2002–2008 (2014)
8. D. Shukla, P.K. Panigarhi, Appl Opt. **59**, 5851–5863 (2020)
9. D. Shukla, P.K. Panigrahi, Colloids Surf. A Physicochem. Eng. Asp. **629**, 127391 (2021)
10. Y. Asakawa, Nature **261**, 220–221 (1976)
11. S. Laohalertdecha, P. Naphon, S. Wongwises, Renew. Sust. Energ. Rev. **11**, 858–876 (2007)
12. V. Vancauwenberghe, P. Di Marco, D. Brutin, Colloids Surf. A Physicochem. Eng. Asp. **432**, 50–56 (2013)
13. K. Takano, I. Tanasawa, S. Nishio, Int. J. Heat Mass Transf. **37**, 65–71 (1994)
14. K. Takano, I. Tanasawa, S. Nishio, J. Enhanc, Heat Transf. **3**, 73–81 (1996)
15. K. Takano, I. Tanasawa, S. Nishio, J.S.M.E. Int, J. Ser. B Fluids Therm. Eng. **38**, 288–294 (1995)
16. K. Takano, I. Tanasawa, S. Nishio, Int. Heat Transf. Conf. Digital Library (1990)
17. A. Bateni, S. Laughton, H. Tavana, S. Susnar, A. Amirfazli, A. Neumann, J. Colloid Interface Sci. **283**, 215–222 (2005)
18. W. Deng, A. Gomez, Int. J. Heat Mass Transf. **54**, 2270–2275 (2011)
19. M. Gibbons, C. Howe, P. Di Marco, A. Robinson, J. Phys. Conf. Ser. **745**, 032066 (2016)
20. Y. Fan, J. Wang, Y. Huo, Z. Zuo, Proc. Int. Conf. Heat Transf. Fluid Flow. **135**, 1 (2014)
21. H. Xu, J. Wang, J. Tian, Y. Huo, B. Li, D. Wang, W. Zhang, J. Yao, Exp. Therm. Fluid Sci. **126**, 110378 (2021)
22. O. Ahmedou, O. Rouaud, M. Havet, Food Bioproc. Tech. **2**, 240–247 (2009)
23. W. Cao, Y. Nishiyama, S. Koide, J. Food Eng. **62**, 209–213 (2004)
24. T.I. Goodenough, P.W. Goodenough, S.M. Goodenough, J. Food Eng. **80**, 1233–1238 (2007)
25. M. Robinson, I.E.E.J. Trans, Electr. Electron. Eng. IEEJ T. **80**, 143–150 (1961)
26. L. Bin, R. Bennacer, A. Bouvet, Appl. Therm. Eng. **31**, 3792–3798 (2011)
27. B.K. Mishra, P. Panigrahi, Phys. Fluids. **32**, 087112 (2020)

28. A. Gupta, B.K. Mishra, P. Panigrahi, Phys. Fluids. **33**, 117118 (2021)
29. M. Takeda, H. Ina, S. Kobayashi, JosA. **72**, 156–160 (1982)
30. R.M. Goldstein, H.A. Zebker, C.L. Werner, Radio Sci. **23**, 713–720 (1988)
31. S. Ma, H. Gao, L. Wu, Appl. Opt. **47**, 1350–1357 (2008)
32. W. Gardiner Jr., Y. Hidaka, T. Tanzawa, Combust. Flame. **40**, 213–219 (1981)
33. G. Hassan, H. El-Kashef, B. El-Baradie, M. El-Labban, Opt. Mater. **5**, 327–332 (1996)
34. S. Karpov, I. Krichtafovitch, Excerpt from the Proceedings of the COMSOL Multiphysics User's Conference 2005 Boston (2005)
35. F.W. Peek, *Dielectric phenomena in high voltage engineering* (McGraw-Hill Book Company, Incorporated, 1920)
36. N. A. Kaptsov, Gas discharge physics (In Russian), Moscow, P: OGIZ. (1947)